Effect of thermal insulation on microstructural homogeneity and onset temperature of flash sintered materials

Ana G. Storion[1*]; Isabela R. Lavagnini[1]; João V. Campos[1]; João G. P. da Silva[2], Sylma C. Maestrelli[3]; Eliria M. J. A. Pallone[1,4]

[1]Postgraduate Programme in Materials Science and Engineering, University of São Paulo, USP/FZEA, Av. Duque de Caxias Norte, 225, 13635-900 - Pirassununga, Brazil.
[2] Forschungszentrum Jülich, Institute for Energy and Climate Research (IEK-1), 52425 Jülich, Germany.
[3]Federal University of Alfenas, José Aurelio Vilela, 11999, Cidade Universitária, BR 267, Km 533, Poços de Caldas, MG, 37715-400, Brazil
[4]Department of Biosystem Engineering, Faculty of Animal Science and Food Engineering (FZEA), University of São Paulo (USP), 13635-900, Pirassununga, SP, Brazil

*Corresponding author at Department of Biosystems Engineering, University of São Paulo, 225 Duque de Caxias Norte Ave, Pirassununga, SP 13635-900, Brazil
E-mail address: anagstorion@usp.br (A.G. Storion)
Phone: +5535999362986 / +551935656712 Fax: +551935654117

Abstract

The present work aimed to reduce the microstructure heterogeneity inherent to flash sintering by using alumina blankets as a thermal insulator around ZnO cylindrical samples during the sintering process, under different electric field conditions. Thermal insulation significantly reduced the flash onset temperature and the grain size heterogeneity. For higher electric fields, a temperature reduction as high as 480ºC was observed, which also led to lower densification. These findings were discussed in terms of changes in the heat loss dynamics coupled with the adsorbed water retention, both promoted by the applied thermal insulation. A model to estimate the temperature at stage III of flash sintering was proposed. The final temperature reached with thermal insulation did not differ significantly from the ones without it. Thus, thermal insulation could represent an alternative route to flash sinter materials with lower furnace temperatures with energy savings up to 78% and a more homogeneous microstructure.

Keywords: Flash Sintering, microstructure evolution, zinc oxide, thermal insulation, grain size.

Introduction

Since it was reported [1], the Flash Sintering process (FS) has been widely investigated in different materials [2–10]. The technique consists of applying an electric field directly through the sample to facilitate sintering. At a specific combination of temperature and electric field, the current that flows through the sample rises abruptly and heats it quickly by Joule heating. At this point, the sample shrinks rapidly, reducing the sintering time from hours to just a few seconds at a furnace temperature much lower than those used in conventional sintering.

Despite the various advantages, one of the challenges for the application of FS on an industrial scale is the microstructural heterogeneity that the consolidated material presents [11,12], mostly reported for samples with a high specific area/volume ratio (e.g., cylindrical samples) [6,13–17]. To avoid this undesired heterogeneity, changes in the flash sintering setup have been proposed, such as Two-Step Flash Sintering (TSFS) [14,18], Current-Ramp Flash Sintering (CRFS) [13,19,20], and Thermally-Insulated Flash Sintering (TIFS) [21–23].

As a recent technique, a thorough microstructural investigation of materials submitted to TIFS is still on its first steps. Only Biesuz et al. (2019) [22] and Wang et al. (2019) [23] have reported improved results concerning microstructural homogeneity and densification using this technique. The insulating material placed around the sample decreases the thermal gradients that occur due to heat loss, mainly by radiation on the material surface [24–26]. In this way, the entire sample tends to remain at a higher temperature, which improves its densification despite producing larger grains. However, until now, TIFS has been performed only for dog-bone samples, which are known for the absence of microstructural heterogeneity due to its low specific area/volume ratio [22,23].

Studying the flash sintering dynamics in geometries with a higher specific area/volume ratio (e.g., cylindrical configurations) can contribute to overcoming the challenges to scale up this technique for ceramics industries. So, the study of TIFS in cylindrical shape becomes essential to investigate if this technique is suited to avoid the microstructure heterogeneity since it is expected higher thermal gradients in this geometry compared to dog-bone shaped ones. Thus, focusing on filling this gap, this work aimed to evaluate the microstructural evolution of cylindrical ZnO samples submitted to TIFS. We also investigated the influence of thermal insulation on the most commonly studied flash sintering aspects, such as onset furnace temperature, power density and electrical conductivity behavior, final sample temperature, and densification. To support some of the proposed discussions, we developed a model for sample temperature estimation in TIFS.

Experimental Procedure

Cylindrical samples with 5 mm in height and 6 mm in diameter were prepared using 99.8% ZnO commercial powder (70 nm - Synth®). The powder was ball-milled in alcohol with 0.5% wt. 4-aminobenzoic acid (PABA, Vetec Ltd.) for 6 h (ball-to-powder mass ratio of 4:1). Then, 0.5% wt. oleic acid (Vetec Ltd.) was added and ball-milled for another 2 h. The resulting suspension was dried under continuous airflow until the total elimination of alcohol and then sifted through an 80-mesh sieve. The samples were isostatically pressed under 200 MPa. The organics were burned out at 500°C for 1 h at a heating rate of 2°C.min^{-1}. The FS and TIFS experiments were carried out in a tubular furnace adapted to perform FS [6]. The limits used for FS experiments of current density (J), electric field (E), and frequency were: 100 and 200 mA.mm^{-2} (RMS basis), 60 – 480 V.cm^{-1} (RMS basis) in alternating current (AC) mode, and 1000 Hz (sinusoidal waveform), respectively. Since no conductive pastes were used, a mechanical pressure of 300 kPa was applied to maintain the contact between the electrodes and the sample. We kept the power supply on after reaching the current density limit (steady-state of FS) for 60 s. The TIFS experiments were performed using the same electrical parameters of FS, differed by the adapted insulation system based on the work of Biesuz et al. (2019)[22].

Figure 1 represents the differences between FS and TIFS setups. In the latter, the electrodes and the cylindrical sample are inserted in an alumina crucible with holes in its ends for the platinum wires contact and thermocouple insertion. After establishing contact between the samples and the electrodes, the crucible was filled with an alumina blanket for insulation, so that the sample remains surrounded by the thermal blanket to reduce heat dissipation to the surroundings. For both experiments (TIFS and FS), a thermocouple was placed at an 8 mm distance from the sample. In TIFS, the set “sample + thermocouple” was also surrounded by alumina blanket, with no insulation medium between the thermocouple and the sample.

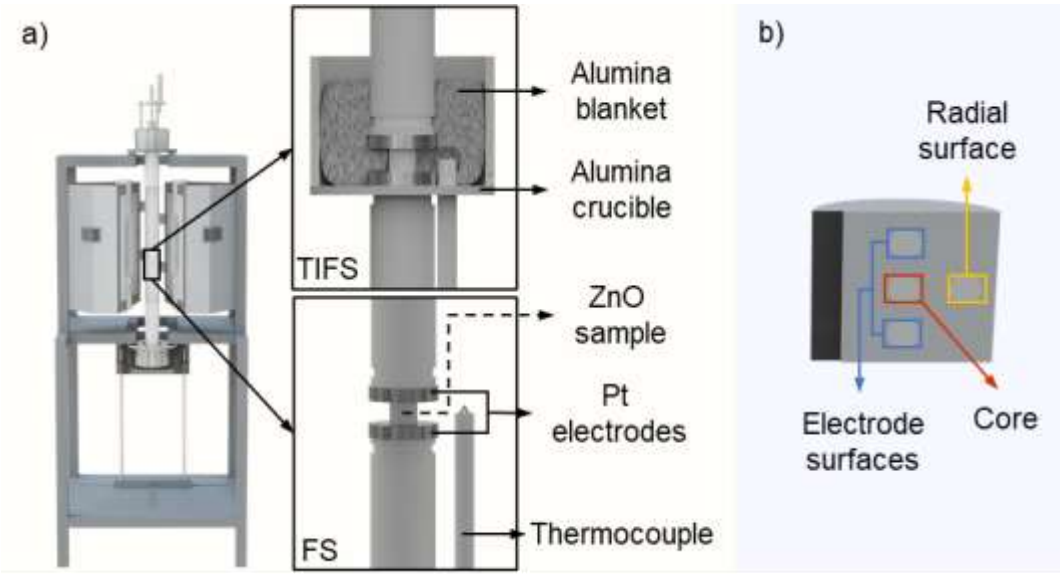

Figure 1 - Experimental setup of the (a) tubular adapted furnace designed for FS and TIFS conditions, and (b) regions for microstructural analysis.

The sample's apparent density was determined by the Archimedes' principle (ASTM C373-88, 2006), and the final density values were described in terms of ZnO theoretical density (5.606 g.cm^{-3}). Thermogravimetric analysis (TGA 4000; PerkinElmer) was performed under synthetic air atmosphere with a flow rate of 20 mL.min^{-1}, and a heating rate of 20ºC.min^{-1} (the same heating hate used in the flash sintering experiments).

Scanning electron microscopy (SEM; Philips, FEG XL30) was used for microstructural characterization of samples fracture surfaces. The grain size distribution was measured by analyzing four different regions according to Figure 1(b): near the upper and lower electrodes, at the core, and the radial surface. For a representative measurement, at least 300 grains of each region were measured. The microstructural homogeneity was evaluated by the Tukey test with a significance level of 5%, assuming similarity between the grain size averages.

Since thermal insulation was used to avoid thermal loss by radiation, the estimated temperature reached by the sample was not able to be calculated by the Black Body Radiation model (BBR) [27]. Therefore, a model to estimate the temperature reached by the sample at stage III of FS was proposed considering the heat loss promoted by conduction and convection mechanisms.

Results and Discussion

Figure 2 presents the results of the furnace onset temperature for each condition studied for FS and TIFS experiments and illustrates the comparison between these results. Table S1,

found in the Supplementary Material, describes the values for each condition. For lower electric field limits, the TIFS leads to a less expressive, although significant, onset temperature difference. However, as the electric field is increased and a certain limit is exceeded, TIFS onset temperature decreased drastically when compared to the FS experiments. Besides, the flash onset temperature tends to decrease as the electric field increases, although this behavior is more tenuous for FS than for TIFS.

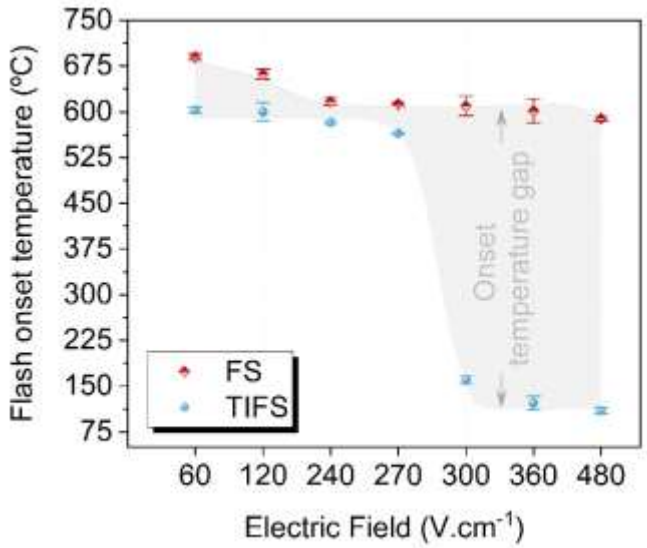

Figure 2 - Graphical representation of the flash onset temperature of FS and TIFS for each studied condition.

Figure 3 shows the final densities obtained for each studied condition with FS and TIFS (the values are expressed in Table S2, in the Supplementary Material). Two distinct zones can be noticed: zone I, where the TIFS procedure improved densification, and zone II, where the TIFS presents less densification when compared to the same condition of FS. To check if the temperature reached by each condition is responsible for the final density differences, the temperature at stage III was calculated according to the proposed model, as follows.

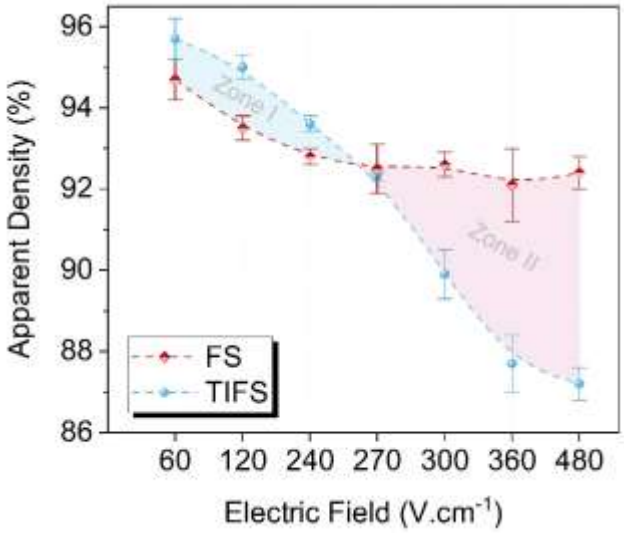

Figure 3 - Graphic comparison between the final density obtained by FS and TIFS for each studied condition.

For the estimation of the temperature distribution, a steady-state heat transfer model with internal heat generation was used:

$$\frac{1}{r}\frac{dT}{dr}\left(\kappa r\frac{dT}{dr}\right)+\dot{q}=0 \tag{1}$$

In equation (1) T is the temperature, r is the radial coordinate, κ is the thermal conductivity and $\dot{q}$ represents the volumetric power dissipation by Joule heating.

Even knowing that ceramic materials are not isotropic due to some characteristics like grain boundaries, packing inhomogeneities, pores, etc., for the sake of simplicity, the thermal conductivity was assumed to be isotropic. So, the equation is solvable by integration and the general solution is:

$$T(r)=-\frac{\dot{q}}{4\kappa}r^2+C_1\ln(r)+C_2 \tag{2}$$

C_1 and C_2 are integration constants, depending on the boundary conditions.

In the middle of the sample, the symmetry boundary condition was used:

$$\left.\frac{dT}{dr}\right|_{r=0}=0 \tag{3}$$

Which in turn, leads to C_1= 0.

In order to determine the value of C_2, for this case, the following boundary condition regarding convection to the furnace was used:

$$\left.\frac{dT}{dr}\right|_{r=r_0}=-\frac{h}{A_s}(T-T_0) \tag{4}$$

In (4), h is the effective convection transfer coefficient, A_s the superficial area of the cylinder, r_0 the full radius of the sample, and T_0 the furnace temperature. Substituting the values in the equation leads to:

$$C_2 = T_0 + \frac{\dot{q} r_0}{2\kappa}\left(\frac{A_s}{h} + \frac{r_0}{2}\right) \tag{5}$$

And the final temperature profile was obtained:

$$T(r) = T_0 - \frac{\dot{q}}{4\kappa} r^2 + \frac{\dot{q} r_0}{2\kappa}\left(\frac{A_s}{h} + \frac{r_0}{2}\right) \tag{6}$$

For the temperature evolution inside the insulation blanket, a steady-state heat transfer model with a temperature-dependent thermal conductivity $\kappa(T)$ was used:

$$\frac{1}{r}\frac{dT}{dr}\left(\kappa(T)\, r \frac{dT}{dr}\right) = 0 \tag{7}$$

Using a linear function for the thermal conductivity:

$$\kappa(T) = \kappa_s T + \kappa_0 \tag{8}$$

$$\frac{d}{dr}\kappa(T) = \kappa_s \frac{dT}{dr} \tag{9}$$

Since now κ depends on the temperature, the outside derivative needs to be computed using the multiplication rule for differentiation. Substituting (9) and (8) in (7):

$$\kappa(T)\frac{d^2T}{dr^2} + \kappa(T)\frac{1}{r}\frac{dT}{dr} + \kappa_s\left(\frac{dT}{dr}\right)^2 = 0 \tag{10}$$

The general solution for this differential equation is:

$$T(x) = \frac{\sqrt{\kappa_s C_3 \ln(r) + \kappa_s C_4 + \kappa_0^2} - \kappa_0}{\kappa_s} \tag{11}$$

C_3 and C_4 are integration constants.

To find the values of C_3 and C_4, the following boundary condition was used:

$$\left.\frac{dT}{dr}\right|_{r=r_{ins}} = -\frac{h}{A_s}(T - T_0) \tag{12}$$

Regarding convection at the outer surface of the insulation layer.

Disregarding thermal resistance in the contact layer, continuity of the temperature and the gradient was assumed in order to fill the other continuity conditions:

$$\left.\frac{dT}{dr}\right|_{r=r_0,sample} = \left.\frac{dT}{dr}\right|_{r=r_{0,insulation}} \tag{13}$$

$$T(r)|_{r=r_0,sample} = T(r)|_{r=r_{0,insulation}} \tag{14}$$

This leads to a system of 3 equations with 3 variables to be determined:

$$\frac{C_3}{2r_0\sqrt{\kappa_s C_3 \ln(r_i) + \kappa_s C_4 + \kappa_0^2}} = -\frac{h}{A_s}\left(\frac{\sqrt{\kappa_s C_3 \ln(r_i) + \kappa_s C_4 + \kappa_0^2} - \kappa_0}{\kappa_s} - T_0\right) \tag{15}$$

$$\frac{C_3}{2r_0\sqrt{\kappa_s C_3 \ln(r_0) + \kappa_s C_4 + \kappa_0^2}} = -\frac{r_0\dot{q}}{2\kappa} \tag{16}$$

$$\frac{\sqrt{\kappa_s C_3 \ln(r_0) + \kappa_s C_4 + \kappa_0^2} - \kappa_0}{\kappa_s} = C_2 - \frac{{r_0}^2\dot{q}}{4\kappa} \tag{17}$$

Solving the system:

$$C_2 = \frac{{r_0}^2\dot{q}}{4\kappa} - \frac{\kappa C_3}{{r_0}^2\dot{q}\kappa_s} \tag{18}$$

$$C_4 = \frac{\kappa^2 C_3^2}{{r_0}^4\dot{q}^2\kappa_s} - \frac{\kappa_0^2}{\kappa_s} - C_3\ln(r_0) \tag{19}$$

The expansion needed to determine the value of C_3 is too large to be written down here, but doable with symbolic computation software. It can be approximated by ignoring the higher order terms by being:

$$C_3 = -\frac{\dot{q}^2{r_0}^3\kappa_s(A_{si} + 2hr_0(\ln(r_i) - \ln(r_0)))}{3h\kappa^4} \tag{20}$$

Once its value is determined, C_2 and C_4 follow.

Then, for the temperature profile inside the sample:

$$T(r) = -\frac{\dot{q}}{4\kappa}r^2 + \frac{{r_0}^2\dot{q}}{4\kappa} + \frac{\dot{q}r_0(A_{si} + 2hr_0(\ln(r_i) - \ln(r_0)))}{3h\kappa^3} \tag{21}$$

Observing the difference between the temperature profiles, they possess the same quadratic dependence on r, and the only difference is the constant term, depending on the heat transfer conditions. Therefore, the profile will only be shifted by a linear term. The constant term can be easily defined as the temperature in the interior of the sample (r=0).

$$T(0)_u = T_0 + \frac{\dot{q}r_0}{2\kappa}\left(\frac{A_s}{h} + \frac{r_0}{2}\right) \tag{22}$$

$$T(0)_i = \frac{{r_0}^2 \dot{q}}{4\kappa} + \frac{\dot{q} r_0 (A_{si} + 2hr_0(\ln(r_i) - \ln(r_0)))}{3h\kappa^3} \quad (23)$$

Where $T(r)_u$ are the temperatures without insulation and $T(r)_i$ are the temperatures with insulation. The temperature difference between both conditions can be determined as:

$$\Delta T = \frac{\dot{q} r_0 (A_{si} + 2hr_0(\ln(r_i) - \ln(r_0)))}{3h\kappa^3} - T_0 - \frac{\dot{q} r_0}{2\kappa} \frac{A_s}{h} \quad (24)$$

Of course, in this case, it was assumed a temperature difference for the same power volumetric dissipation.

Figure 4 summarizes the temperatures calculated by the model for the FS and TIFS experiments and compares the differences between the furnace temperature and the estimated temperature at stage III. Table S2 (Supplementary Material) reports the calculated temperature values and the final densities for each studied condition. It is noticed that for lower electric fields, both the furnace and the estimated temperatures barely differ between FS and TIFS. For higher electric fields, although, large differences in furnace temperature were associated with small differences in the estimated temperature. This stands for the ability of thermal insulation to compensate and optimize heat loss. Therefore, even at lower furnace temperature, the insulation allows the sample to reach temperatures similar to those in FS without insulation (with higher onset temperatures). Also, following Figure 3 and Figure 4, since the final temperature reached is lower for higher electric fields when using TIFS, it results in a slightly lower final density when compared to FS.

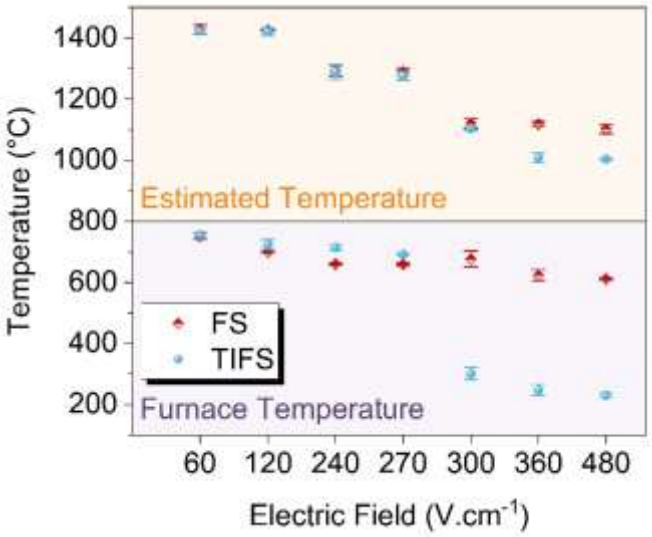

Figure 4 - Stage III average furnace and estimated sample temperatures for FS and TIFS.

The flash onset occurs when a critical combination of temperature and electric field is reached, triggering the thermal runaway. In this cycle, there is a continuous increase in the sample's temperature and its electrical conductivity, due to Joule heating. This cycle continues until the current reaches the pre-established limit and the power supply switches to current control [28].

According to Campos et al. (2020) [15], the sample temperature at the beginning of the flash event is determined by an energy balance between the dissipated power and the heat loss to the environment, whether by conduction, convection, and/or radiation. Since the convection contribution is reduced due to the thermal insulation provided by the alumina blanket, the heat loss due to this mechanism becomes negligible. Furthermore, in TIFS experiments, the difference in temperature between the sample and alumina blanket (used for insulation) becomes less significant, also contributing to the minimization of heat loss by radiation. This fact justifies the decrease in the flash onset temperature since the dissipated power becomes more intensely absorbed by the sample when the heat loss becomes minimized. However, the expected reduction in the onset temperature caused by different heat transfer conditions should shift the onset temperatures in a uniform way, such as seen from 60 to 270 $V.cm^{-1}$.

To investigate the reason for the existence of the different zones shown in Figure 3, which have an abrupt change in flash onset on values higher than 270 $V.cm^{-1}$, the Arrhenius plot of electric power density and electrical conductivity (Figure 5) was investigated in more detail. Those curves present distinct behaviors concerning FS and TIFS. For lower electric fields, such as 60 $V.cm^{-1}$ and 120 $V.cm^{-1}$, the curves presented the typical behavior observed in FS samples. For these same electric field thresholds, the electrical conductivity curves are maintained at the same levels. However, for higher electric fields applied to the sample, the curves start to behave quite differently. For FS, in the temperature range between approximately 230 to 350°C, there is an increase in electrical conductivity, which leads to an increase in the dissipated electric power density. However, this increase was not high enough to promote the flash event. As the temperature continues to rise, from 550°C onward, the second increase in electrical conductivity occurs, which immediately triggers the flash event.

In the case of TIFS, the use of higher electric fields provides a similar phenomenon, but with higher intensity. In the approximate temperature range of 170 to 250°C, there is an increase in the electrical conductivity which may cause only a power peak (shoulder) or may trigger the flash event (depending on the electric field limits). The anticipated flash happens for electric fields above 270 $V.cm^{-1}$. From this point, the non-linear increase of electrical conductivity

favors the thermal runaway, and the flash event occurs. It can be seen that TIFS has provided a decrease of at least 480°C in the flash onset temperature for the highest electric field condition.

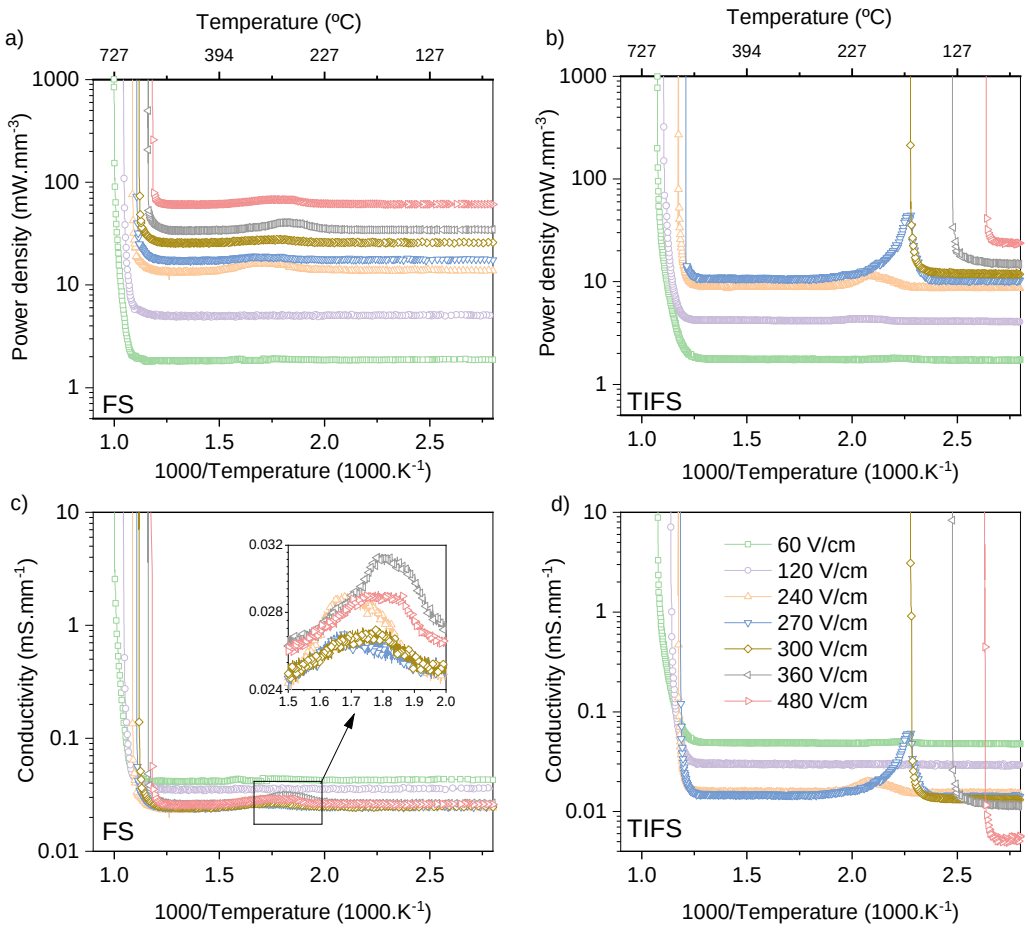

Figure 5 - Arrhenius plot of the electric power density and electrical conductivity for FS and TIFS for each studied condition.

It is well established in the literature that for ZnO, in temperatures up to 300ºC, the loss of chemically adsorbed water occurs [29,30]. Many ZnO applications such as heterogeneous photocatalysis, hydrogen production, and gas sensors [31,32] derive from the strong interaction of its surface with ambient water, which has a significant influence on the surface stability and electronic properties of a semiconductor [33,34]. Nevertheless, the role of water on the densification during sintering is still not completely clear [35–38]. Varela et al. (1990) [39] firstly suggested that water chemically interacts with the ZnO surface and dissociates into H^+ and OH^-. This interaction leads to the formation of surface defects and increases surface diffusion.

Some authors have used the positive aspects of the interaction between aqueous solutions with different materials to aid their densification processes [40–42]. Funahashi et al. (2016)

[42] firstly applied the Cold Sintering Process to ZnO by using acetic acid solution and uniaxial press, changing the sintering temperature from values below 300ºC. Dargatz et al. (2016) [43] sintered dry and wet powders of ZnO by FAST/SPS sintering and stated there is a heating rate dependence for the water content to be high enough to affect the sintering behavior [43,44]. Nie et al. (2018) [45] reported the Water-Assisted Flash Sintering, in which the absorbed water vapor can trigger FS in ZnO cylindrical samples by increasing its electrical conductivity. The authors also stated that the water effects can persist until approximately 350°C. Kermani et al. (2020) [36] also demonstrated the benefits of combining water, external pressure, and electric field in a process named Flash Cold Sintering to optimize the densification of ZnO with the absence of external heating.

Meanwhile, the shoulder on the ZnO power density and electrical conductivity plots before the "normal" FS temperature has not been reported in previous literature so far. To investigate whether the possible reasons for this peak appearance could be related to adsorbed water, additional experiments were performed. Figure 6 demonstrates flash sintering experiments with different heating steps, wherein in Figure 6(a) the temperature rises in a constant heating ramp, with the electric field applied since the beginning of the heating. The power density curve shows the appearance of a peak around 170°C, which has not triggered the flash event, also in agreement with the graphs in Figure 5. Figure 6 (b) demonstrates the same electric field conditions, but differing for an isothermal stage at 300°C for 2 h, followed by cooling to 80°C and subsequent constant heating rate until the flash event. It is noted that the same peak appears on the first heating stage, identical to the one presented in Figure 6(a). However, no peak appeared on the cooling nor the second heating stage. Figure 6(c) differs from Figure 6(b) only by the time of the application of the electric field. In the latter, the electric field was applied only at the second heating stage. It is noted that no peak of power density appeared in this condition.

These setups exclude the fact that this shoulder is related to the field-effect on the material of a specific phenomenon that happens at this temperature since under two heating stages the peak only appeared in the first one. Thermal analysis (Figure S1 – Supplementary Material) shows two weight losses, the first one around 200ºC and the second one around 350ºC. The TG curve continued to drop until the final temperature. This process can be explained by the desorption of water as a gradual process for ZnO since the dissociated ions (H^+ and OH^-) can be trapped in pore-particles contacts, neck formations, and grain boundaries [43,46]. Since the sample was already free of organics, all the mass losses were attributed respectively to

physically adsorbed water and OH^- loss. From the TGA, the total water loss after the second drop is around 1,05%.

Kermani et al. (2020) [36] were able to trigger flash sintering in ZnO at room temperature by using 60 $V.cm^{-1}$ and 23wt.% water under a 20 MPa mechanical load. When cold sintering ZnO at 126ºC by using acetic acid as an aqueous solution (20wt.%) without the use of electric fields, higher pressures (387 MPa) and longer sintering time (1 h) were necessary to achieve nearly full densification [42]. Schwarz et al. (2012) [46] used high heating rates (100 $K.min^{-1}$) when coupling FAST/SPS sintering and humid conditions (the powder was stored in an 85% humidity environment) to densify ZnO in 400ºC and 50 MPa. The latter used lower humidity, with less than 1wt.% loss up to 500ºC.

Dargatz et al. (2016) [43] stated that amounts of water as low as 0.1% is sufficient to influence the ZnO sintering behavior, although the authors found that 1.6% was the ideal humidity for the optimized densification under FAST/SPS Sintering with a mechanical load of 50 MPa. Gonzalez-Julian et al. (2018) [35], using the same condition reported in [43], increased the applied pressure to 150 MPa and were able to reduce the sintering temperature to 250ºC. The authors affirmed that only small quantities of water are required to influence the sintering of ZnO since all the contributions come from the adsorbed molecules. Some of the effects of the adsorbed water are the dissociation into H^+ and OH^- which will diffuse into the crystal structure and lead to the formation of defects at the grain boundaries and/or particle interfaces and enhancement of diffusion rates and mass transport [35,43,44].

Therefore, the shoulder presented in Figure 5 could be related to the presence of adsorbed water. When sintered via TIFS, the physical barrier promoted by the insulation blanket acts by trapping water vapor and also enhancing the absorption of the dissipated power (by thermally insulating the material and reducing the heat loss). These facts can lead to an increase in the electrical conductivity and promote a temperature rise to a point that, from a critical electric field value, it may trigger the flash event. In the experimental setup, we were able to achieve densification levels comparable to those presented in the literature with lower values of both mechanical load and humidity, which were 300 kPa and 1.05%, respectively. Although the influence of water on FS has been reported before [35–38,45], its effects have been intensified by thermal insulation without the need to use an experimental apparatus designed for this principle. Also, the process can be applied to different geometries since there is no need to use a mold to apply external pressure (the pressure applied was only for maintaining the electrical contact). The use of the thermal blanket, besides being easy to manage, can also optimize the time and energy consumption of the sintering.

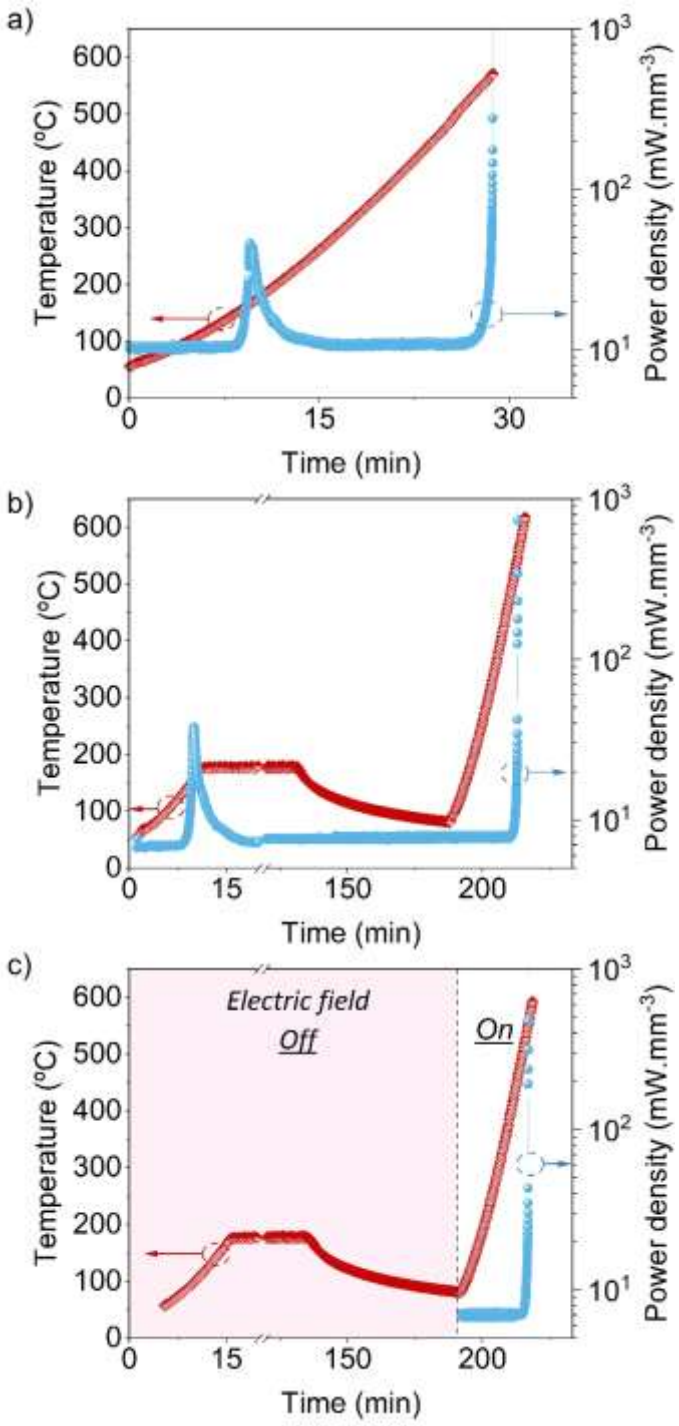

Figure 6 - *Curves of heating ramp (°C) and power density (mW.mm^{-3}) of TIFS experiments under E=270 V.cm^{-1} and J=200 mA.mm^{-2} for (a) constant heating ramp with the electric field applied since the beginning; (b) two stages of heating ramp interspersed by an isothermal plateau with the electric field applied since the first heating stage; (c) two stages of heating ramp interspersed by an isothermal plateau with the electric field applied from the second heating stage.*

To evaluate the effect of the thermal insulation on the microstructure, Figure 7 presents the SEM micrographs for three regions: near the electrodes, core, and radial surface of the samples sintered using E = 60 and 480 $V.cm^{-1}$ and J = 200 $mA.mm^{-2}$. Table 1 presents the average grain sizes for each analyzed region. For the samples sintered by TIFS technique, there is a tendency for the grain size to be bigger when compared to the same conditions using FS technique. This fact is due to the thermal insulation, where the heat loss is reduced, especially by radiation. Hence, the TIFS samples remain under high temperatures for a longer period, leading to grain growth. Moreover, a higher electric field led to smaller grain sizes, except for the FS480 core region. This happens due to the lower final temperature reached by this sample, according to the proposed model (Figure 4).

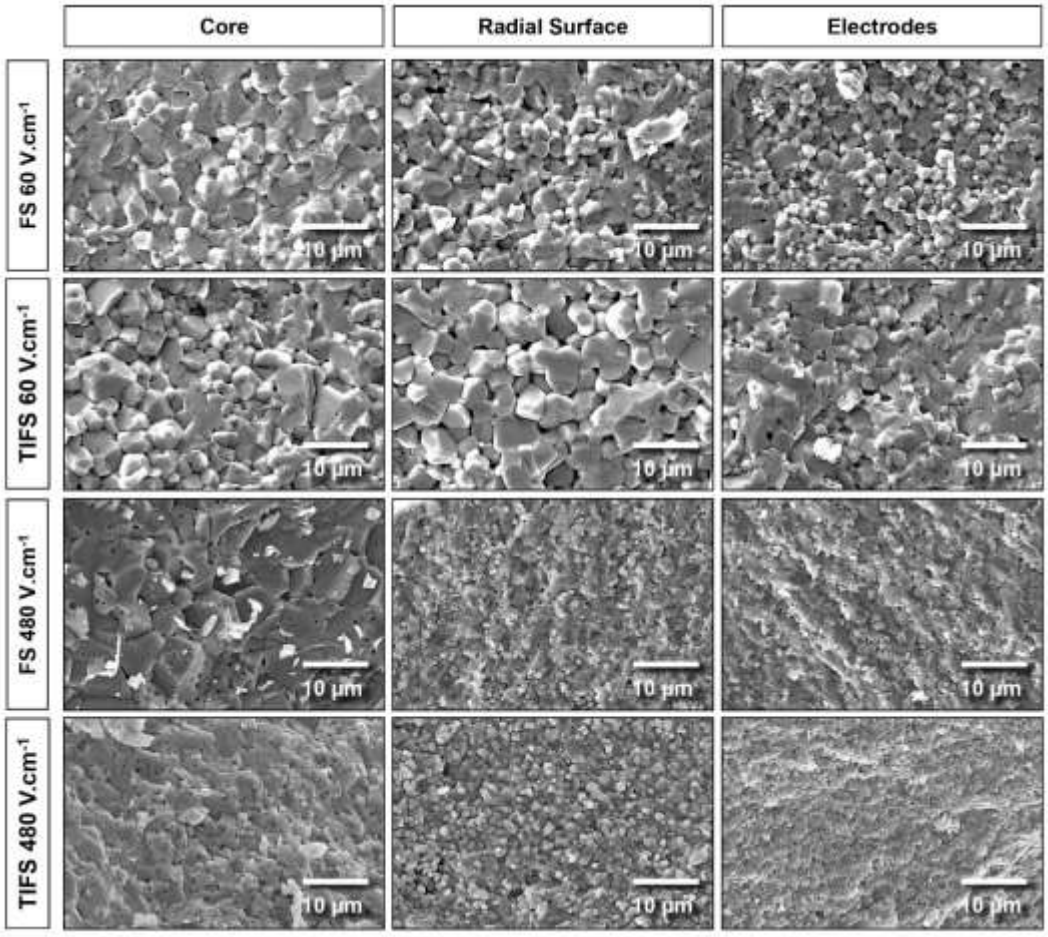

Figure 7 - SEM images of three different regions: near the electrodes, core, and radial surface of FS and TIFS samples using E=60 and 480 $V.cm^{-1}$ and J=200 $mA.mm^{-2}$.

	Core	Radial Surface	Electrodes
FS60	3.10±0.80	2.17±0.46	1.32±0.33
TIFS60	3.75±0.67	3.59±0.65	1.69±0.53
FS480	4.59±0.98	1.10±0.21	0.74±0.18
TIFS480	1.75±0.38	1.09±0.22	0.95±0.18

Table 1 - Average grain size (µm) of three different regions: near the electrodes, core, and radial surface of FS and TIFS samples using E=60 and 480 V.cm^{-1} and J=200 mA.mm^{-2}.

Tukey Mean Difference plot, Figure 8, was performed to better analyze the microstructure heterogeneity/homogeneity in function of the different conditions studied. The names in Figure 8 are presented according to the following: the region analyzed, the sintering method, and the electric field used; for example, the radial surface region of the sample sintered by TIFS with 60 V.cm^{-1} was named as RS-TIFS60. Tukey Mean Difference plot gives an idea of the samples' degree of heterogeneity/homogeneity. The further away from x = 0, the more heterogeneous the sample is when compared to the others.

For FS conditions all regions were statistically different, while for TIFS the microstructural homogeneity was more pronounced. The samples flash sintered under 480 V.cm^{-1} showed the most heterogeneous microstructure, with the grain size at the core reaching around five times the grain size of the other regions. Meanwhile, for the TIFS at the same electric field condition, this difference is reduced. This condition showed the smaller microstructure heterogeneity, in which the radial surface and the electrode regions presented no statistical differences and the core and the radial surface and the core and the electrode regions presented minimized differences.

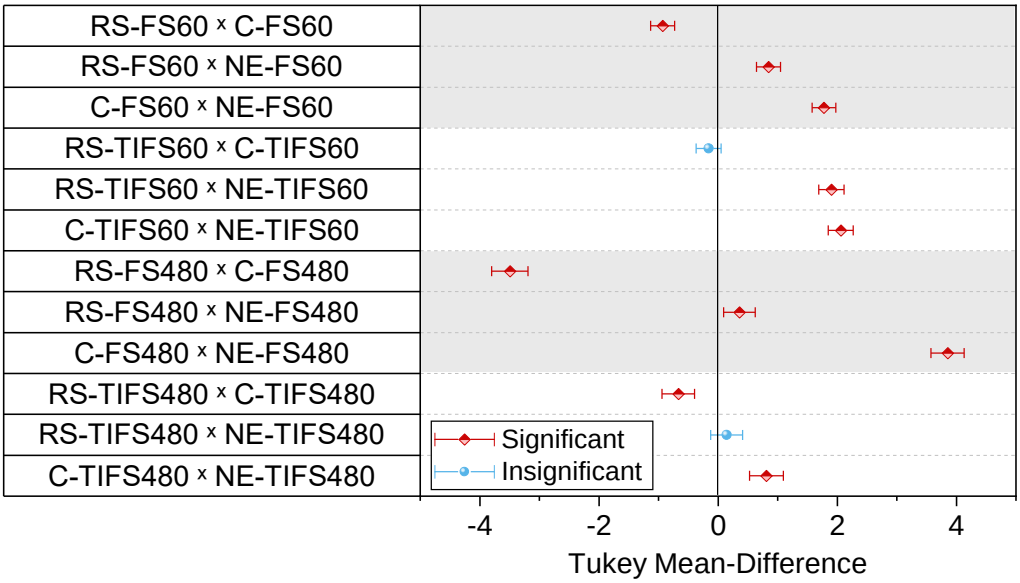

Figure 8 - Tukey Mean-Difference of grain size with 5% of significance level for three different regions: near the electrodes (NE), core (C), and radial surface (RS) of FS, and TIFS samples using E=60 and 480 V.cm^{-1} and J=200 mA.mm^{-2}.

The pronounced microstructural heterogeneity presented by the FS samples under 480 V.cm^{-1} can be explained by hotspot formation that might occur under higher electrical conditions. Nevertheless, thermal insulation allows better microstructural homogeneity in the radial direction of the sample. However, the heat loss contribution from the conduction mechanism due to the electrode is still significant. In that way, the region near the electrodes presents the smallest grain sizes for all the studied conditions.

The differences in temperature between the core of the sample and the furnace become more intense under higher electric fields, which can lead to thermal stress and heterogeneous densification, leading to failure of the sample. Since these differences were mitigated using thermal insulation, the TIFS technique presents an attractive way to get around such problems commonly reported by the scientific flash sintering community. The existence of the shoulder in the conductivity curves of TIFS for ZnO can provide an anticipatory route of the flash event to lower temperatures at intermediate electric field limits. Wang et al. (2019) [23] were able to perform FS of ZnO at temperatures below 100°C, however, using a higher electric field of 2800 V.cm^{-1}. Also, the authors used a dog-bone shaped sample and were able to reach 92% of final density. Besides that, a microstructure with exacerbated grain growth was also reported by the authors. This fact can be explained by a combination of electric field and current density that form a critical point which, below this point, the safe zone of the FS occurs, and above, the failure zone occurs [47].

For high electric fields (~10^3 V.cm^{-1}), hotspots formations could be induced leading to local overheating and possibly melting the material, forming microstructural heterogeneity. According to Campos et al. (2020) [15], hotspots occur mainly in cylindrical samples, due to their higher area/volume ratio, leading to larger density gradients within the sample [15,25,26,48]. Although the densification provided by the TIFS was lower than FS for the higher electric field limits (300, 360, 480 V.cm^{-1}), it could be solved by increasing the current density or the time of the flash event. This lower density can be correlated to the lower calculated steady-state temperature by the proposed model.

By considering the power consumed by the furnace and the power supply during the experiments, the energy consumption of the FS and TIFS processes could be compared (the calculus for this estimation is found in the Supplementary Material). For low electric field values, since the flash onset temperature is almost unchanged (according to Figure 4 and Table S2), the energy consumed by both processes barely differs. For these conditions, the advantage of TIFS is due to improved microstructural homogeneity and higher densification. For higher electric field values, where the anticipatory path is favored, energy savings with the use of TIFS reached values up to 78%. Therefore, in addition to the microstructural control, TIFS may also be attractive for industrial applications due to the considerable reduced energy consumption in sintering.

Conclusions

In this study, we showed that TIFS was able to decrease the flash onset temperature of ZnO. Regarding the final density of the samples, TIFS experiments provided two different behaviors: (1) using low electric field limits, TIFS improved densification even reducing the flash onset temperature; (2) using high electric field limits, the temperature reduction was high enough to result in less densification. Besides temperature reduction, TIFS provided a more homogeneous microstructure, reducing the difference in grain size between the core and the radial surface in FS to barely no difference with the use of TIFS technique.

The proposed model for calculating the estimated temperature in stage III of FS considered the contribution of heat loss mechanisms in general, not only radiation. When also considering that the thermal insulation provided by an insulating blanket (whose constant k depends on the internal and external temperature), the model was able to provide a better insight into the estimated temperature that the sample reaches. TIFS in addition to providing a decrease of 450ºC in furnace onset temperature, also managed to reach an estimated temperature during stage III only 100ºC lower than the one achieved for FS under the same conditions, evidencing

the improved energy savings with the insulation process (up to 78% compared with FS experiments without insulation).

We also showed that the presence of absorbed water within the sample could anticipate the flash event at much lower temperatures when using high electric field limits (above 270 $V.cm^{-1}$). This effect is more expressive in TIFS experiments.

Acknowledgments

The authors thank the São Paulo Research Foundation (FAPESP) [2018/11143-0; 2018/04331-5; 2019/14677-9], the Coordenação de Aperfeiçoamento de Pessoal de Nível Superior - Brasil (CAPES) - Finance Code 001 and the National Council for Scientific and Technological Development (CNPq) [200573/2018-7].

References

[1] M. Cologna, B. Rashkova, R. Raj, Flash sintering of nanograin zirconia in <5 s at 850°C, J. Am. Ceram. Soc. 93 (2010) 3556–3559. https://doi.org/10.1111/j.1551-2916.2010.04089.x.

[2] R. Muccillo, E.N.S. Muccillo, Electric field-assisted flash sintering of tin dioxide, J. Eur. Ceram. Soc. 34 (2014) 915–923. https://doi.org/10.1016/j.jeurceramsoc.2013.09.017.

[3] L.M. Jesus, R.S. Silva, R. Raj, J.C. M'Peko, Electric field-assisted flash sintering of CaCu3Ti4O12: Microstructure characteristics and dielectric properties, J. Alloys Compd. 682 (2016) 753–758. https://doi.org/10.1016/j.jallcom.2016.05.002.

[4] A.M. Raftery, J.G.P. da Silva, D.D. Byler, D.A. Andersson, B.P. Uberuaga, C.R. Stanek, K.J. McClellan, Onset conditions for flash sintering of UO2, J. Nucl. Mater. 493 (2017) 264–270. https://doi.org/10.1016/j.jnucmat.2017.06.022.

[5] K. Ren, Q. Wang, Y. Lian, Y. Wang, Densification kinetics of flash sintered 3mol% Y2O3 stabilized zirconia, J. Alloys Compd. 747 (2018) 1073–1077. https://doi.org/10.1016/j.jallcom.2018.02.308.

[6] J.V. Campos, I.R. Lavagnini, R.V. de Sousa, J.A. Ferreira, E.M. de J.A. Pallone, Development of an instrumented and automated flash sintering setup for enhanced process monitoring and parameter control, J. Eur. Ceram. Soc. 39 (2019) 531–538. https://doi.org/10.1016/j.jeurceramsoc.2018.09.002.

[7] C.A. Grimley, A.L.G. Prette, E.C. Dickey, Effect of boundary conditions on reduction during early stage flash sintering of YSZ, Acta Mater. 174 (2019) 271–278. https://doi.org/10.1016/j.actamat.2019.05.001.

[8] D. Schwarzbach, J. Gonzalez-Julian, O. Guillon, V. Roddatis, C.A. Volkert, Towards In-Situ Electron Microscopy Studies of Flash Sintering, Ceramics. 2 (2019) 472–487. https://doi.org/10.3390/ceramics2030036.

[9] C. Cao, R. Mücke, O. Guillon, Effect of AC field on uniaxial viscosity and sintering stress of ceria, Acta Mater. 182 (2020) 77–86. https://doi.org/10.1016/j.actamat.2019.10.035.

[10] B. Yoon, V. Avila, R. Raj, L.M. Jesus, Reactive flash sintering of the entropy-stabilized oxide Mg0.2Ni0.2Co0.2Cu0.2Zn0.2O, Scr. Mater. 181 (2020) 48–52. https://doi.org/10.1016/j.scriptamat.2020.02.006.

[11] M. Biesuz, V.M. Sglavo, Flash sintering of ceramics, J. Eur. Ceram. Soc. 39 (2019) 115–143. https://doi.org/10.1016/j.jeurceramsoc.2018.08.048.

[12] A.G. Storion, J.A. Ferreira, S.C. Maestrelli, E.M. de J.A. Pallone, Influence of the forming method on flash sintering of ZnO ceramics, Ceram. Int. 47 (2021) 965–972. https://doi.org/10.1016/j.ceramint.2020.08.210.

[13] M.K. Punith Kumar, D. Yadav, J.M. Lebrun, R. Raj, Flash sintering with current rate: A different approach, J. Am. Ceram. Soc. 102 (2018) 1–13. https://doi.org/10.1111/jace.16037.

[14] I.R. Lavagnini, J. V. Campos, E.M.J.A. Pallone, Microstructure evaluation of 3YSZ sintered by Two-Step Flash Sintering, Ceram. Int. (2021). https://doi.org/10.1016/j.ceramint.2021.04.174.

[15] J. V Campos, I.R. Lavagnini, J.G.P. da Silva, J.A. Ferreira, R. V Sousa, R. Mücke, O. Guillon, E.M.J.A. Pallone, Flash sintering scaling-up challenges: Influence of the sample size on the microstructure and onset temperature of the flash event, Scr. Mater. 186 (2020) 1–5. https://doi.org/10.1016/j.scriptamat.2020.04.022.

[16] M.C. Steil, D. Marinha, Y. Aman, J.R.C. Gomes, M. Kleitz, From conventional ac flash-sintering of YSZ to hyper-flash and double flash, J. Eur. Ceram. Soc. 33 (2013) 2093–2101. https://doi.org/10.1016/j.jeurceramsoc.2013.03.019.

[17] E.N.S. Muccillo, S.G.M. Carvalho, R. Muccillo, Electric field-assisted pressureless sintering of zirconia–scandia–ceria solid electrolytes, J. Mater. Sci. 53 (2018) 1658–1671. https://doi.org/10.1007/s10853-017-1615-3.

[18] J. Nie, Y. Zhang, J.M. Chan, S. Jiang, R. Huang, J. Luo, Two-step flash sintering of ZnO: Fast densification with suppressed grain growth, Scr. Mater. 141 (2017) 6–9. https://doi.org/10.1016/j.scriptamat.2017.07.015.

[19] H. Charalambous, S.K. Jha, K.H. Christian, R.T. Lay, T. Tsakalakos, Flash sintering

using controlled current ramp, J. Eur. Ceram. Soc. 38 (2018) 3689–3693. https://doi.org/10.1016/j.jeurceramsoc.2018.04.003.

[20] I. R. Lavagnini, J.V. Campos, J.A. Ferreira, E.M. de J.A. Pallone, Microstructural evolution of 3YSZ flash-sintered with current ramp control, J. Am. Ceram. Soc. 103 (2020) 3493–3499. https://doi.org/10.1111/jace.17037.

[21] Y. Dong, I. -We. Chen, Thermal Runaway in Mold-Assisted Flash Sintering, J. Am. Ceram. Soc. 99 (2016) 2889–2894. https://doi.org/10.1111/jace.14413.

[22] M. Biesuz, J. Dong, S. Fu, Y. Liu, H. Zhang, D. Zhu, C. Hu, S. Grasso, Thermally-insulated flash sintering, Scr. Mater. 162 (2019) 99–102. https://doi.org/10.1016/j.scriptamat.2018.10.042.

[23] X. Wang, Y. Zhu, R. Huang, H. Mei, Z. Jia, Flash sintering of ZnO ceramics at 50 °C under an AC field, Ceram. Int. 45 (2019) 24909–24913. https://doi.org/10.1016/j.ceramint.2019.08.142.

[24] Y. Dong, I.W. Chen, Electrical and hydrogen reduction enhances kinetics in doped zirconia and ceria: II. Mapping electrode polarization and vacancy condensation in YSZ, J. Am. Ceram. Soc. 101 (2018) 1058–1073. https://doi.org/10.1111/jace.15274.

[25] J. Park, I.W. Chen, In situ thermometry measuring temperature flashes exceeding 1,700°C in 8 mol% Y2O3-stablized zirconia under constant-voltage heating, J. Am. Ceram. Soc. 96 (2013) 697–700. https://doi.org/10.1111/jace.12176.

[26] K. Terauds, J.M. Lebrun, H.H. Lee, T.Y. Jeon, S.H. Lee, J.H. Je, R. Raj, Electroluminescence and the measurement of temperature during Stage III of flash sintering experiments, J. Eur. Ceram. Soc. 35 (2015) 3195–3199. https://doi.org/10.1016/j.jeurceramsoc.2015.03.040.

[27] R. Raj, Joule heating during flash-sintering, J. Eur. Ceram. Soc. 32 (2012) 2293–2301. https://doi.org/10.1016/j.jeurceramsoc.2012.02.030.

[28] R.I. Todd, E. Zapata-Solvas, R.S. Bonilla, T. Sneddon, P.R. Wilshaw, Electrical characteristics of flash sintering: thermal runaway of Joule heating, J. Eur. Ceram. Soc. 35 (2015) 1865–1877. https://doi.org/10.1016/j.jeurceramsoc.2014.12.022.

[29] I. Perelshtein, A. Lipovsky, N. Perkas, A. Gedanken, E. Moschini, P. Mantecca, The influence of the crystalline nature of nano-metal oxides on their antibacterial and toxicity properties, Nano Res. 8 (2015) 695–707. https://doi.org/10.1007/s12274-014-0553-5.

[30] N. Mayedwa, A.T. Khalil, N. Mongwaketsi, N. Matinise, Z.K. Shinwari, M. Maaza, The Study of Structural, Physical and Electrochemical Activity of ZnO Nanoparticles Synthesized by Green Natural Extracts of Sageretia Thea, Nano Res. Appl. 03 (2017) 1–

9. https://doi.org/10.21767/2471-9838.100026.

[31] T. Kaewmaraya, B. Pathak, C.M. Araujo, A.L. Rosa, R. Ahuja, Water adsorption on ZnO(10$\bar{1}$0): The role of intrinsic defects, Epl. 97 (2012) 1–6. https://doi.org/10.1209/0295-5075/97/17014.

[32] S. Kenmoe, P. Ulrich Biedermann, Water aggregation and dissociation on the ZnO(1010) surface, Phys. Chem. Chem. Phys. 19 (2017) 1466–1486. https://doi.org/10.1039/c6cp07516a.

[33] H. Ye, G. Chen, H. Niu, Y. Zhu, L. Shao, Z. Qiao, Structures and mechanisms of water adsorption on ZnO(0001) and GaN(0001) surface, J. Phys. Chem. C. 117 (2013) 15976–15983. https://doi.org/10.1021/jp312847r.

[34] T.B. Rawal, A. Ozcan, S.H. Liu, S.V. Pingali, O. Akbilgic, L. Tetard, H. O'Neill, S. Santra, L. Petridis, Interaction of Zinc Oxide Nanoparticles with Water: Implications for Catalytic Activity, ACS Appl. Nano Mater. 2 (2019) 4257–4266. https://doi.org/10.1021/acsanm.9b00714.

[35] J. Gonzalez-Julian, K. Neuhaus, M. Bernemann, J.G.P. da Silva, A. Laptev, M. Bram, O. Guillon, Unveiling the mechanisms of cold sintering of ZnO at 250 °C by varying applied stress and characterizing grain boundaries by Kelvin Probe Force Microscopy, Acta Mater. 144 (2018) 116–128. https://doi.org/10.1016/j.actamat.2017.10.055.

[36] M. Kermani, M. Biesuz, J. Dong, H. Deng, M. Bortolotti, A. Chiappini, M.J. Reece, V.M. Sglavo, C. Hu, S. Grasso, Flash cold sintering: Combining water and electricity, J. Eur. Ceram. Soc. 40 (2020) 6266–6271. https://doi.org/10.1016/j.jeurceramsoc.2020.06.051.

[37] M. Biesuz, G. Taveri, A.I. Duff, E. Olevsky, D. Zhu, C. Hu, S. Grasso, A theoretical analysis of cold sintering, Adv. Appl. Ceram. 119 (2020) 75–89. https://doi.org/10.1080/17436753.2019.1692173.

[38] I.R. Lavagnini, J.V. Campos, A.G. Storion, A.O. Lobo, R. Raj, E.M. de J.A. Pallone, Influence of flash sintering on phase transformation and conductivity of hydroxyapatite, Ceram. Int. 47 (2021) 9125–9131. https://doi.org/10.1016/j.ceramint.2020.12.036.

[39] J.A. Varela, O.J. Whittemore, E. Longo, Pore size evolution during sintering of ceramic oxides, Ceram. Int. 16 (1990) 177–189. https://doi.org/10.1016/0272-8842(90)90053-I.

[40] J. Guo, H. Guo, A.L. Baker, M.T. Lanagan, E.R. Kupp, G.L. Messing, C.A. Randall, Cold Sintering: A Paradigm Shift for Processing and Integration of Ceramics, Angew. Chemie - Int. Ed. 55 (2016) 11457–11461. https://doi.org/10.1002/anie.201605443.

[41] J. Guo, S.S. Berbano, H. Guo, A.L. Baker, M.T. Lanagan, C.A. Randall, Cold Sintering

Process of Composites: Bridging the Processing Temperature Gap of Ceramic and Polymer Materials, Adv. Funct. Mater. 26 (2016) 7115–7121. https://doi.org/10.1002/adfm.201602489.

[42] S. Funahashi, J. Guo, H. Guo, K. Wang, A.L. Baker, K. Shiratsuyu, C.A. Randall, Demonstration of the cold sintering process study for the densification and grain growth of ZnO ceramics, J. Am. Ceram. Soc. 100 (2017) 546–553. https://doi.org/10.1111/jace.14617.

[43] B. Dargatz, J. Gonzalez-Julian, M. Bram, P. Jakes, A. Besmehn, L. Schade, R. Röder, C. Ronning, O. Guillon, FAST/SPS sintering of nanocrystalline zinc oxide-Part I: Enhanced densification and formation of hydrogen-related defects in presence of adsorbed water, J. Eur. Ceram. Soc. 36 (2016) 1207–1220. https://doi.org/10.1016/j.jeurceramsoc.2015.12.009.

[44] B. Dargatz, J. Gonzalez-Julian, M. Bram, Y. Shinoda, F. Wakai, O. Guillon, FAST/SPS sintering of nanocrystalline zinc oxide-Part II: Abnormal grain growth, texture and grain anisotropy, J. Eur. Ceram. Soc. 36 (2016) 1221–1232. https://doi.org/10.1016/j.jeurceramsoc.2015.12.008.

[45] J. Nie, Y. Zhang, J.M. Chan, R. Huang, J. Luo, Water-assisted flash sintering: Flashing ZnO at room temperature to achieve ~ 98% density in seconds, Scr. Mater. 142 (2018) 79–82. https://doi.org/10.1016/j.scriptamat.2017.08.032.

[46] S. Schwarz, A.M. Thron, J. Rufner, K. Van Benthem, O. Guillon, Low temperature sintering of nanocrystalline zinc oxide: Effect of heating rate achieved by field assisted sintering/spark plasma sintering, J. Am. Ceram. Soc. 95 (2012) 2451–2457. https://doi.org/10.1111/j.1551-2916.2012.05205.x.

[47] F. Trombin, R. Raj, Developing processing maps for implementing flash sintering into manufacture of whiteware ceramics, Am. Ceram. Soc. Bull. 93 (2014) 32–35.

[48] Y. Dong, H. Wang, I.W. Chen, Electrical and hydrogen reduction enhances kinetics in doped zirconia and ceria: I. grain growth study, J. Am. Ceram. Soc. 100 (2017) 876–886. https://doi.org/10.1111/jace.14615.